Structural origin of recovered ferroelectricity in BaTiO₃ nanoparticles

H. Zhang [1], S. Liu,[1] S. Ghose [2], B. Ravel,[3] I. U. Idehenre,[4,5] Y. A. Barnakov [4,5,6] S. A. Basun,[4,5]
D. R. Evans,[4,*] and T. A. Tyson [1,†]

[1]*Department of Physics, New Jersey Institute of Technology, Newark, New Jersey 07102, USA*
[2]*National Synchrotron Light Source II, Brookhaven National Laboratory, Upton, New York 11973, USA*
[3]*National Institute of Standards and Technology, Gaithersburg, Maryland 20899, USA*
[4]*Air Force Research Laboratory, Materials and Manufacturing Directorate, Wright-Patterson Air Force Base, Ohio 45433, USA*
[5]*Azimuth Corporation, 4027 Colonel Glenn Highway, Beavercreek, Ohio 45431, USA*
[6]*IPG Photonics Corporation, Southeast Technology Center, Birmingham, Alabama 35211, USA*

Nanoscale BaTiO₃ particles ($\approx$10 nm) prepared by ball-milling a mixture of oleic acid and heptane have been reported to have an electric polarization several times larger than that for bulk BaTiO₃. In this work, detailed local, intermediate, and long-range structural studies are combined with spectroscopic measurements to develop a model structure of these materials. The x-ray spectroscopic measurements reveal large Ti off-centering as the key factor producing the large spontaneous polarization in the nanoparticles. Temperature-dependent lattice parameter changes manifest sharpening of the structural phase transitions in these BaTiO₃ nanoparticles compared to the pure nanoparticle systems. Sharp crystalline-type peaks in the barium oleate Raman spectra suggest that this component in the composite core-shell matrix, a product of mechanochemical synthesis, stabilizes an enhanced polar structural phase of the BaTiO₃ core nanoparticles.

I. INTRODUCTION

Perovskite barium titanate BaTiO₃ is a classical ferroelectric perovskite material known since the 1940s, and has a well-defined structure-property relationship. It undergoes several phase transitions upon cooling from high temperature, including a high-symmetry paraelectric cubic to tetragonal ferroelectric phase at 393 K, a transition to an orthorhombic ferroelectric phase at 278 K, and a transition to a rhombohedral ferroelectric phase at 183 K. The key mechanisms of such structural transformations are based on cation displacements and oxygen octahedra rotations around different axes of the high-symmetry parent cubic phase. In the bulk system, the off-centering of Ti and O ions from the high symmetry positions in the cubic phase drives the ferroelectric state.

With reduced size, perovskite nanoparticles often possess unique electronic, optical, and magnetic properties compared to their bulk form [1–3]. Nanoparticles have very promising potential usage in many areas, including data storage, biorelated imaging, and targeted drug delivery [4]. Classical theoretical models predict that as the particle size is reduced, the transition temperature and ferroelectric polarization should be reduced monotonically [5–11], as has been demonstrated experimentally [11]. BaTiO₃ has also been reported to have a linearly ordered and monodomain polarization state at nanometer dimensions, as well as room-temperature spontaneous polarization down to particles of size

$\sim$10 nm [2] in cube-shaped particles. However, the piezoelectric coefficient (d_{33}) in these particles is found to be $\approx$ 2% of the bulk value.

It was later proposed and experimentally demonstrated that ball-milling of micron-sized BaTiO₃ powder in oleic acid and heptane resulted in small nanoparticles ($\approx$ 10 nm) with an extremely large spontaneous polarization [12–16]. This "top-down" approach is explicitly suitable for ferroelectric materials, where the ferroelectric properties could be substantially modified by mechanical means: pressure and shear [10]. Previous work involved doping of a liquid crystal (LC) host with ball-milled BaTiO₃ nanoparticles, which reported on a class of nematic ferroelectric LC nanocolloidal suspension [17–20]. Systematic electrical characterization of nanoparticles ball-milled in a mixture of heptane and oleic acid revealed up to a fivefold enhancement of the spontaneous polarization (yielding values of $100-120 \, \mu\text{C}/\text{cm}^2$) at room temperature [12,15]. More recent work has provided support for crystalline barium oleate being responsible for maintaining the ferroelectric properties of BaTiO₃ nanoparticles (i.e., spontaneous polarization of $130 \, \mu\text{C}/\text{cm}^2$), which is formed in a mechanochemical reaction during ball-milling [16,21]. In particular, in Ref. [16], it was inferred from spectroscopic studies that nanosized BaTiO₃ particles ($\approx$ 10 nm) and mechanochemically synthesized crystalline barium oleate formed from oleic acid in a mechanochemical reaction during ball-milling form a core-shell type structure; it was suggested that the interface of the crystalline shell and core particle was the source of surface stress. It was argued that the presence of such a crystalline shell plays the crucial role in the maintenance and even an enhancement of ferroelectricity on the

*Corresponding author: dean.evans@afrl.af.mil
†Corresponding author: tyson@njit.edu

064106-1

nanoscale. It was suggested that the core-shell structure is created via the formation of specific bonding between surface atoms of the nanoparticle and carboxylate ions of organic ligands at the interface, which results in a lattice mismatch between the crystalline shell and core [17]. Note that the core-shell systems described in Refs. [16,21] are used for the work described in this current paper; they are also very similar in nature to the materials that were investigated in Refs. [10,12,14,15,17–20]. No direct structural measurement has yet been given in support of the existence of the core-shell model. The previous studies suggest a model mechanism but provide no direct structural proof.

Although it is known that these nanoscale materials exhibit an electric polarization significantly exceeding bulk values [12,15,16], prior to this work direct structural information (such as bond length changes, distortions, and structural changes with temperature) has not been available for this system. This current work aims to provide a detailed understanding of the atomic-level structure of the final nanoparticles prepared using the ball-milling process (i.e., the mechanochemical synthesis process). This will help enable the development of a general approach for the stabilization and enhancement of the ferroelectric state in bulk systems when the size is reduced to the nanoscale. The primary results of the analysis in this work is that a significant Ti off-centering is present concomitant with the appearance of polar phonon modes and a ratio of $BaTiO_3$ to barium oleate of 0.7 ± 0.1:1.0 is found, suggesting a coating of the $BaTiO_3$ particles by the crystalline barium oleate.

II. SAMPLE PREPARATION, EXPERIMENTAL APPROACH, AND MODELING METHODS

The 10-nm nanoparticles were prepared by mechanical ball-milling commercial bulk $BaTiO_3$ for 25 h in heptane and oleic acid using a Retsch[1] planetary high energy ball-mill (PM 200) with zirconia crucibles and 2-mm zirconia beads. The ratio of $BaTiO_3$, oleic acid, and heptane used was 1:1:20 by weight [14]. The final particle size was determined by transmission electron microscopy (TEM) as well as powder x-ray diffraction (XRD) refinement. In this work, the particle diameter from ball-milling was determined to be 9 ± 2 nm (using the Scherrer method [22] within a Rietveld refinement [23]; see Supplemental Material Fig. S3 and Table S1 [24]). The primary samples used in the measurements were washed with anhydrous ethanol to remove excess unreacted freestanding oleic acid/carboxylate from the colloidal suspension. The Supplemental Material [24] presents data for both washed and as-prepared samples. Unmilled $BaTiO_3$ nanoparticles with 700- and 50 nm diameter (actual size is 70 ± 3 nm (Scherrer method); see Table S1 [24]) were purchased commercially from Alfa Aesar and are used as reference samples. The un-

milled 700 nm $BaTiO_3$ is considered to be a bulk standard in this work. Commercial barium oleate (Alfa Aesar) was milled and used as a reference sample.

Laboratory XRD measurements were combined with synchrotron-based diffraction and spectroscopy experiments to determine the structural details of this system. More details on the specific measurement systems and modeling used, as well as detailed Raman measurements and x-ray diffraction modeling, can be found in the Supplemental Material [24].

III. RESULTS AND DISCUSSION

A. Raman measurements

The results from Raman measurements are shown in Fig. 1 and in Figs. S4 and S5 of the Supplemental Material [24]. Figure 1 shows the room temperature Raman spectra for the unmilled 700-nm (bulk) and 50-nm reference samples and the milled 10-nm $BaTiO_3$. Also shown in Fig. 1 are data for barium oleate; for comparison, oleic acid data are presented in Fig. S4 [24] (taken from Ref. [25]). Note that the oleic acid starting material is converted to a metal carboxylate (i.e., barium oleate) during the ball-milling process via mechanochemical synthesis [16,21].

The arrow in Fig. 1(a) reveals that for both the 50- and 10-nm samples, there is an additional peak near $190\,cm^{-1}$, which is not present in the 700-nm (bulk) sample indicating a reduction in symmetry. This feature is known to become enhanced in the rhombohedral low-temperature phase in bulk samples (below ≈ 183 K) with micron-scale grains, but it is evident in these nanoparticles at room temperature. This peak corresponds to an $A1$ (TO) mode in the tetragonal system as seen by Marssi *et al.* in Ref. [26], which is significantly sharpened in the 10-nm sample. These modes are characteristic of a polar phase in perovskite systems and their strong enhancement indicates a profound symmetry reduction in the 10-nm sample consistent with polar-type space groups.

It can also be seen that there are additional peaks in the spectra of the 10-nm sample, and a strong similarity in peaks in the barium oleate sample above $\approx 800\,cm^{-1}$ [see Fig. 1(b) and Figs. S4 and S5 of the Supplemental Material], which are not present in the 50- and 700-nm samples. Note that oleic acid also shows similarities to this (see Figs. S4 and S5), but there are significant deviations over the range $800 - 1200\,cm^{-1}$. The high intensity of these features in the 10-nm sample indicates the presence of a significant contribution of organic components. A complete set of measurements for all samples between 50 and $3400\,cm^{-1}$ is shown in Supplemental Material Figs. S4 and S5.

The assignment of the aforementioned spectral features is as follows: the high-frequency peaks are due to light atoms and hence the spectra at these frequencies do not provide information of bonding to heavy atoms (such as the Ti or Ba atoms in the starting material); in systems containing carbon chains, the C-C single bonds generate modes near $1000\,cm^{-1}$, while double-bonded carbon produces modes near $1600\,cm^{-1}$ [27]; peaks near $\approx 3000\,cm^{-1}$ correspond to C-H bonds. Incidentally, the set of features that show a significant difference between the samples is over the range $1000–1150\,cm^{-1}$ [Fig. S4(b)]; in this case, the barium oleate sample shows
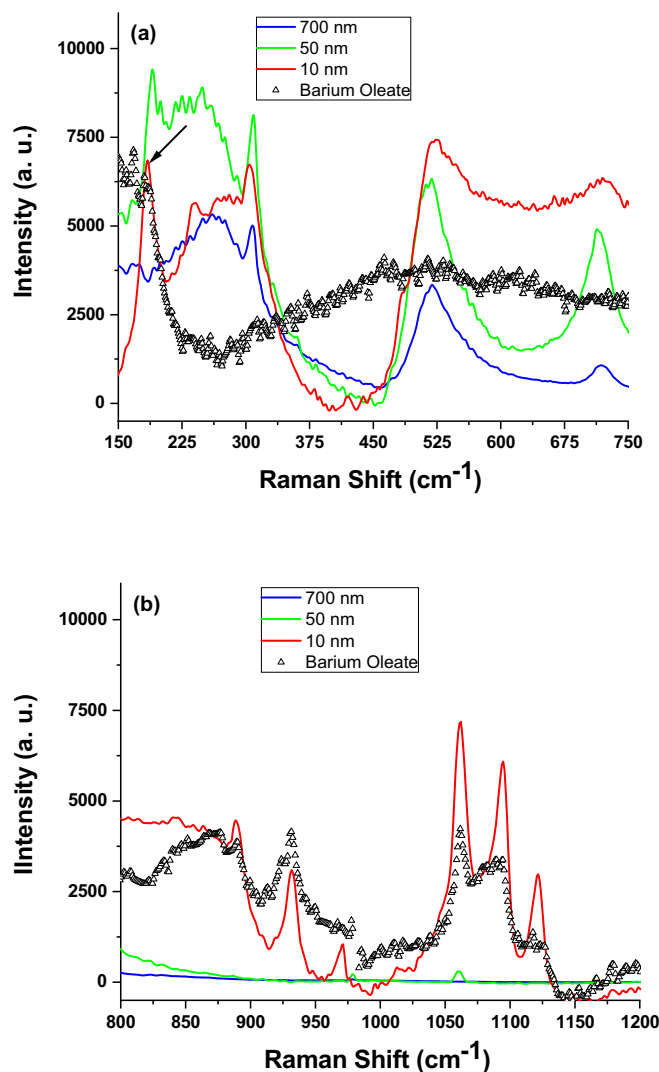

FIG. 1. Room temperature Raman measurements for 700-nm bulk (blue), 50-nm (green), and milled 10-nm (red) $BaTiO_3$ samples are compared with barium oleate (black open triangles). Spectra are shown for the range (a) $150-750 \, cm^{-1}$ and (b) the higher energy region $800-1200 \, cm^{-1}$. Data for the range $50-3400 \, cm^{-1}$ are given in Supplemental Material Figs. S4 and S5. Data for the 10-nm samples match barium oleate over the spectral range $800-3400 \, cm^{-1}$ [Fig. 1(b) and Figs. S4 and S5 of the Supplemental Material]. The peaks of the 10-nm sample are significantly sharper, indicating a high degree of crystalline order. The arrow in Fig. 1(a) identifies an additional peak near $190 \, cm^{-1}$ for the 50- and 10-nm samples, indicating a reduction in symmetry; this peak is not present in the 700-nm (bulk) sample. In (b) the 10-nm nanoparticle and barium oleate samples are shown for comparison.

the strongest resemblance to the 10-nm nanoparticles. This suggests that barium oleate may be playing a more significant role in the nanocolloids than the oleic acid; this is in agreement with the Fourier-transform infrared spectroscopy (FTIR) results in Refs. [16] and [21], which demonstrates that nearly all of the oleic acid is converted to a metal carboxylate (i.e., barium oleate) during the milling process via mechanochemical synthesis. For this reason, the discussion below is centered

around barium oleate as the primary organic component in the ferroelectric nanocolloid (milled 10-nm sample).

A comparison of the peaks above $800 \, cm^{-1}$ for the 10-nm nanoparticle and barium oleate samples reveals that all features are present [Fig. 1(b)] for both cases; these features are absent in the unmilled 50- and 700-nm reference samples. The sharpening of the peaks in the 10-nm sample is due to a significantly higher degree of structural order compared to crystalline barium oleate. The results point to a complex $BaTiO_3$/barium oleate composite mixture (possibly a core-shell configuration as suggested in Ref. [16] or nanoparticles embedded in a barium oleate host). Details of the structure were found by systematic x-ray absorption and x-ray pair distribution function measurements, which are preferentially sensitive to heavy atoms (see below).

B. X-ray absorption measurements and simulations (local structure about Ti and about Ba)

Figure 2(a) shows the Ti K-edge x-ray absorption near-edge structure (XANES) for the 700- and 50-nm reference samples compared to the milled 10-nm sample. These spectra are the result of averaging three consecutively measured scans. The statistical variations in the scans are the level of the line thicknesses since these are concentrated samples. The r-space curves in Fig. 2(c) and 2(d) were extracted from the corresponding averaged spectra. The 700- and 50-nm XANES spectra exhibit sharp peaks in the region near 4960 eV [near-threshold; see Fig. 2(a) inset] as expected for bulklike systems with high atomic order, while the 10-nm sample is broadened due to reduction in long-range structural coherence relative to the bulk sample. Focusing on Fig. 2(a), it is seen that the pre-edge peak near 4968 eV (feature A) of the 10-nm sample is broadened (and more intense) compared to both the 700-nm (bulk) and 50-nm samples. This feature is well known to be related to the degree of off-centering of the Ti sites (relative to the cubic structure) in ATiO$_3$ systems concomitant with a polar phase (see Refs. [28–31]). These multiple pre-edge features near ≈ 4970 eV correspond to transitions from a 1s core level to levels composed of hybridized Ti $4p$, Ti $3d$, O $2p$ states (analogous to the well-studied perovskite manganites [32–34]). Feature A in the spectrum corresponds to a transition to the e_g band, and the unlabeled lower energy shoulder (left side of feature A) is related to the t_{2g} band. The e_g peak in the XANES spectra of ATiO$_3$ systems is sensitive to local distortions (i.e., coordination of the Ti sites) and is found to have an integrated intensity proportional to the mean square displacement amplitude of the Ti atom off the ideal (cubic) site [29–31,35]. In Fig. S1 we show that fits of the main pre-edge peaks to a Lorentzian function, which will produce results independent of normalization, indicate that the width and area of the 10-nm sample peak approach values twice that of the corresponding values for the 50-nm peak. Hence the higher intensity of this peak in the 10-nm sample reveal larger off-centering than in the reference samples. This is revealed more clearly by the simulations below.

XANES measurements are most sensitive to local structural changes (disorder and off-centering of Ti), as opposed to a difference in long-range order between orthorhombic and tetragonal structures. For this reason, either tetragonal or
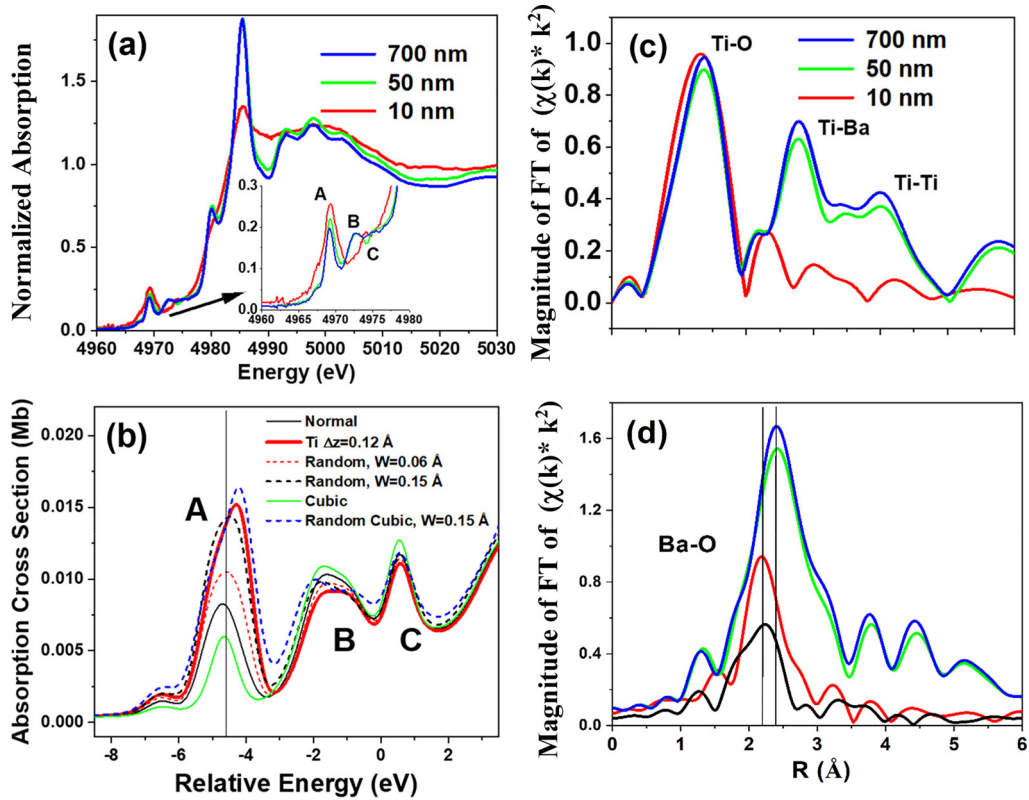
FIG. 2. (a) Curves for Ti K-edge XANES spectra for 10-nm BaTiO$_3$ (red), 50-nm BaTiO$_3$ (green), and 700-nm BaTiO$_3$ (blue). (b) Simulated XANES pre-edge spectra for bulk BaTiO$_3$ (orthorhombic) referred to as "normal," BaTiO$_3$ (orthorhombic) with 0.12-Å z-displacement amplitude, and BaTiO$_3$ (orthorhombic) with random displacements of all atoms with 0.06- and 0.15-Å average values. The spectra of BaTiO$_3$ with no distortion (cubic) and with 0.15-Å average atomic distortion to cubic BaTiO$_3$ are also given. (c) Ti K-edge structure function for 10-nm (red), 50-nm (green), and 700-nm BaTiO$_3$ (blue) samples. Distances are relative to the average titanium atom position. (d) The corresponding Ba L_3 structure functions for the same samples as in part (c). The blue, green, red, and black curves correspond to 700-nm, 50-nm, 10-nm, and barium oleate samples, respectively. Distances are relative to the average barium atom position. Note that (c) utilizes the same x-axis scale and range used in (d). In both (c) and (d), note that $\chi(k)$ is dimensionless while the wave vector k has units of Å^{-1}.

orthorhombic structures can be used to provide insight on local structural changes. Choosing a well-established bulk structure and applying three-dimensional (3D) distortions allows us to capture the local distortions and study the effect of both disorder and local displacements. XANES simulations for the pre-edge region are shown for specific structural changes in Fig. 2(b); see Ref. [28] and the Supplemental Material [24] for computational methods. Simulations were conducted using the RELXAS full multiple scattering code [36]. The Ti K edge core natural width (0.94 eV, full width at half maximum) was included in the simulations [37]. Input structural data used for the simulated phases were taken from Ref. [38]). The results of these simulations produce the XANES pre-edge spectra for the given BaTiO$_3$ input structures with either a 0.12-Å Ti z displacement (amplitude) or with random displacements in x, y, and z directions [with a 3D random displacement of all atoms giving average displacement amplitudes (W) of 0.06 or 0.15 Å]; these displacements are relative to the room temperature orthorhombic atomic positions in the lattice. The spectra of cubic BaTiO$_3$ with no distortion and that for cubic BaTiO$_3$ with a 0.15-Å average atomic distortion are also given as a reference. Note the weakest main peak amplitude (feature A) is obtained for the undistorted cubic phase, while the peak amplitude is signifi-

cantly enhanced for both the Ti off-centering in the "normal" orthorhombic phase and random (incoherent) disorder characteristic of amorphous phases (see amorphous example in Ref. [29]). It is noted that for the case of Ti displacements (Δz), feature A is enhanced while feature B is suppressed. The sample is not cubic since there are polar Raman modes. We also observe that the Raman data reveal no significant peak broadening in the nanoscale material; there is also no evidence of a cubic structure found below in standard XRD or pair distribution function (PDF) measurements. The milled 10-nm sample is not amorphous. As seen in the PDF measurements below, the peaks in the radial distribution function beyond the first shell are not suppressed. Hence, the enhanced peak area of the main pre-edge feature A, seen in the 10-nm BaTiO$_3$ sample compared to bulk BaTiO$_3$, is due to Ti off-centering in a crystalline phase characteristic of the polar ferroelectric state. (It should be noted that the 50-nm reference sample has a weakly enhanced area relative to the 700-nm bulklike sample.)

The extended x-ray absorption fine structure data are consistent with the XANES results. Figure 2(c) shows the Fourier transform of the fine structure over the k range ($2.00 < k < 7.70$ Å^{-1}) for a qualitative comparison. This structure function has peaks that correspond to the atomic shells about

the average Ti site. The results at the Ti K edge indicate a strong Ti-O first shell coordination, but there is a significant reduction of structural order for the second shell Ti-Ba and higher shells in the 10-nm sample (the Ti-Ba and Ti-Ti peaks are suppressed in the 10-nm sample). This reduction is due to structural disorder or lowering of symmetry about the Ti sites (variation in nearest neighbor Ti-Ba and Ti-Ti distances), leading to destructive interference of the higher shell scattering signals. Ti-Ba and Ti-Ti signals with different bond distances interfere destructively and suppress the peak amplitudes. This suggests large structural disorder or highly reduced symmetry in the nanoparticles. Examining Figs. 2(a) and 2(c), it is seen that from the perspective of the Ti sites that new chemical phases containing Ti are not evident. The primary change in the 10-nm sample is the reduction in structural correlation between Ti and higher neighbors beyond O. Combined with the Ti XANES results, the characteristic structural feature of the milled 10-nm sample with respect to bulk (orthorhombic) $BaTiO_3$ is the large Ti off-centering.

For a qualitative comparison, Fig. 2(d) shows the Fourier transform of the fine structure for the Ba $L3$ edge over the k range $1.98\,\text{Å}^{-1} < k < 9.43\,\text{Å}^{-1}$. This structural function has peaks that correspond to the atomic shells about the average Ba site. The 700- and 50-nm reference samples show similar structure relative to Ba sites (as in the case of the Ti site), however, the 10-nm sample has a first shell peak shifted to lower R values. Also shown in Fig. 2(d) are data for barium oleate. We note that the shift and position of the Ba-O first peak in the 10-nm sample are consistent with that of barium oleate (black curve). The results suggest that a significant component of barium oleate is present in the sample, consistent with the Raman results (above) and the FTIR data presented in Ref. [21]. The diffraction measurements in the following paragraph provide strong support for this assertion.

C. Wide angle x-ray diffraction (long-range structure)

Figure 3 shows the results from laboratory XRD measurements, including data for the 10-nm, 50-nm, and barium oleate samples. Barium oleate has peaks primarily below 30 ° (2θ). Further details can be seen by expanding the figure; see Fig. 3(b), where the barium oleate sample is compared with the 10-nm sample; it becomes evident that there is a structure present that is similar to barium oleate, although some of the peak intensities do not fully match. This suggests that a derivative of barium oleate (with minor changes in atomic position) is present and possibly coating the $BaTiO_3$ particles or hosting them in a matrix. Some possible modifications may be due to the formation of chelate or bidentate structures as suggested in Ref. [16].

It is important to note that the sharp Bragg peaks in Figs. 3(a) and 3(b) for the 10-nm $BaTiO_3$ sample indicate that both the milled 10-nm $BaTiO_3$ and the milled "barium oleate" type components are highly crystalline. No broad maxima, typical of amorphous components, are seen in the data. It should also be noted that the peak widths in barium oleate and the 10-nm $BaTiO_3$ samples are quite similar indicating a high degree of crystallinity in the nanoscale material with respect to the heavy atom sites which dominate the x-ray diffraction pattern. To further elucidate the nature of the structure of
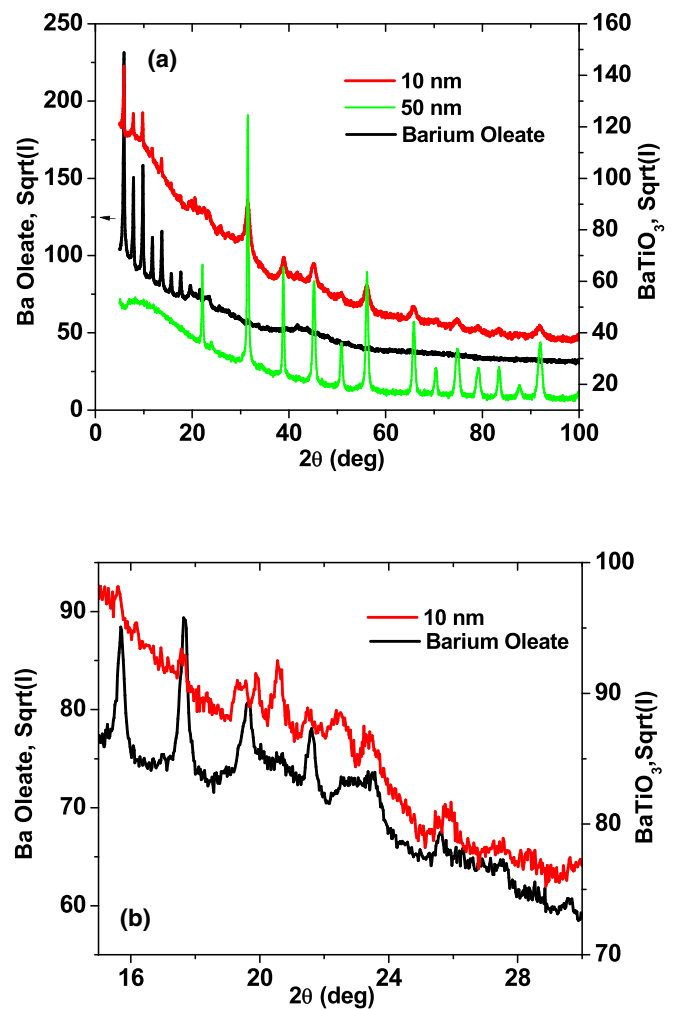

FIG. 3. (a) XRD measurements of the 10-nm (red) and 50-nm (green) samples of $BaTiO_3$ and barium oleate (black). (b) Expanded region between $15°$ and $30°$ in 2Θ for the 10-nm and barium oleate samples.

10-nm $BaTiO_3$ samples for both local ($< \approx 5\,\text{Å}$) and intermediate ranges, x-ray PDF measurements were conducted.

D. Pair distribution function measurements and modeling

Total scattering x-ray PDF measurements (which includes both the Bragg scattering and diffuse scattering due to local distortions) were conducted to investigate the details of the structure [39–42]. The atomic pair distribution functions $G(r)$ are displayed in Fig. 4. Note that $G(r)$ is the reduced pair distribution function, which oscillates about zero and is obtained directly from the scattering data $S(Q)$. $G(r) = \frac{2}{\pi} \int_0^\infty Q[S(Q) - 1]\sin(Qr)dQ$ is related directly to the standard pair distribution function defined as $G(r) = 4\pi r(\rho(r) - \rho_0)$, where $\rho(r)$ is the atomic number density and ρ_0 is the average atomic number density. We note that $\rho(r) = \rho_0 g(r)$ with $g(r)$ being the radial atomic distribution function (see the Supplemental Material text and Fig. 4). In Fig. 4(a), it is seen that for a radius r greater than $\approx 10\,\text{Å}$ the shape of the pair distribution function for the 700-, 50-, and 10-nm samples are fairly similar, although for the 10-nm
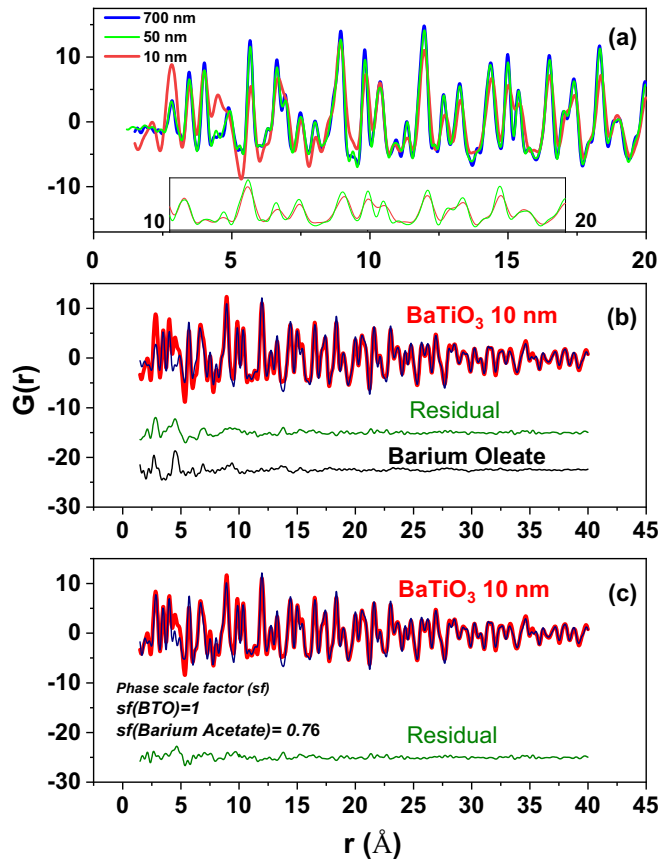
FIG. 4. (a) Experimental PDF $G(r)$ curves for the 700-nm (blue), 50-nm (green), and 10-nm (red) BaTiO$_3$. The inset is the expanded region between 10 and 20 Å. (b) Experimental PDF curve (red), refinement model (blue), and the residual (green) for 10-nm BaTiO$_3$. The experimental PDF curve of barium oleate (black) is shown for comparison. Note the similarity. (c) An additional barium acetate phase was added to the region between 1.5 and 10 Å to model the short-range features of the PDF.

sample, peaks and troughs are broader due to the particle size effect. Below ≈ 10 Å, there is a significant difference between the milled 10-nm sample and the unmilled 50- and 700-nm samples. As in the case of the high-frequency Raman data, laboratory XRD data, and Ba L_3-edge x-ray absorption fine structure (XAFS) data (Figs. 1–3), the difference between the 10-nm sample and the BaTiO$_3$ model indicates the existence of another compound with a significant organic component similar to the barium oleate reference sample. Note that the residual (i.e., the signature of an additional species that is observed when the model fit results are subtracted from the 10-nm BaTiO$_3$ data) has sharp and well-defined peaks below 10 Å indicating that both the BaTiO$_3$ and the extra component (second phase) are highly ordered structurally. Barium oleate was used as a possible second phase by comparison to the residual of the fit of the data to the BaTiO$_3$ model. PDF measurements were conducted under the same conditions as for the BaTiO$_3$ samples.

To obtain a better understanding, structural refinements with models were conducted [43]. Specifically, in order to model the system with a limited set of free parameters, a tetragonal model was utilized. We note that the real system may be orthorhombic. The main point is that the 10-nm system was found to be noncubic (a and c are not equal).

Experimental PDF patterns are shown in Fig. 4(a). Model fits of the region between 10 and 20 Å were conducted for a tetragonal model of BaTiO$_3$. For the 10-nm sample, the refined structural parameters were then used to calculate the $G(r)$ for $r \leqslant 10$ Å; the result is shown in Fig. 4(b). In this panel the red curve is the experimental PDF, the blue curve is the model, and the green curve is the difference between the data and the model (residual). It is clear that the residual profile (data minus the fit for the 10-nm sample) matches well with the $G(r)$ of the barium oleate (black curve).

To quantify the amount of barium oleate relative to BaTiO$_3$, a barium acetate phase structural model (which possesses similar short-range structure to barium oleate) was included in the structural refinement. Hence the model included BaTiO$_3$ and barium acetate (model for barium oleate). The result is shown in Fig. 4(c). As shown in Fig. 4(b), the residual is the difference between the data and the model. The extra features in the low-r range now can all fit well, except for the full amplitude of the nearest neighbor Ba-Ba ≈ 4 Å. The ratio of the two components (BaTiO$_3$ and the barium acetate model) acquired from refinement is 1:0.76, indicating a very significant amount of barium oleate existing in the BaTiO$_3$ 10-nm ball-milled sample. The exact form of barium oleate is not known. However, as seen from the very sharp peaks in the barium oleate component from Raman measurements, it may be bonded to the BaTiO$_3$ nanoparticles. The results suggest that the BaTiO$_3$ particles are coated by barium oleate (consistent with optical data in Ref. [17]) with $\approx 1:1$ BaTiO$_3$. More accurately, the Ba site:Ba site ratio (i.e., barium oleate sites to barium in the core BaTiO$_3$) in both components is $0.7 \pm 0.1:1.0$ (by volume or number of Ba atoms; see the Supplemental Material [24]).

To understand the phase transitions in the BaTiO$_3$ core-shell samples, the lattice parameters derived from temperature-dependent PDF refinements were determined between ≈ 100 and ≈ 500 K. Nonlinear variations in the lattice parameters (or their ratios) are expected at the cubic to tetragonal transition near 393 K, the tetragonal to orthorhombic transition near 278 K, and the orthorhombic to rhombohedral transition near 183 K (see the structural transitions in bulk BaTiO$_3$ in Ref. [37]). Changes (slope changes or discontinuities) are expected at structural phase transitions in the lattice parameter vs temperature curve. In Fig. 5, the temperature dependence of the c/a lattice parameter ratio is given. For the (unmilled) 700-nm reference sample (bulk), inflection points (indicated by arrows) are seen at the appropriate positions for the phase transition temperatures. For the (unmilled) 50-nm reference sample, the transitions are broadened significantly and are indistinguishable. In particular, the low-temperature tetragonal to orthorhombic and orthorhombic to rhombohedral transitions are merged. This broadening of the transition with reduced particle size was observed for free-standing BaTiO$_3$ particles for sizes down to 28 nm in previous work [44,45], where the broadening was assigned to loss of structural coherence of the local distortions. In contrast to the 50-nm sample, the transitions in the milled 10-nm sample are readily visible. Also, a c/a ratio with significant deviations
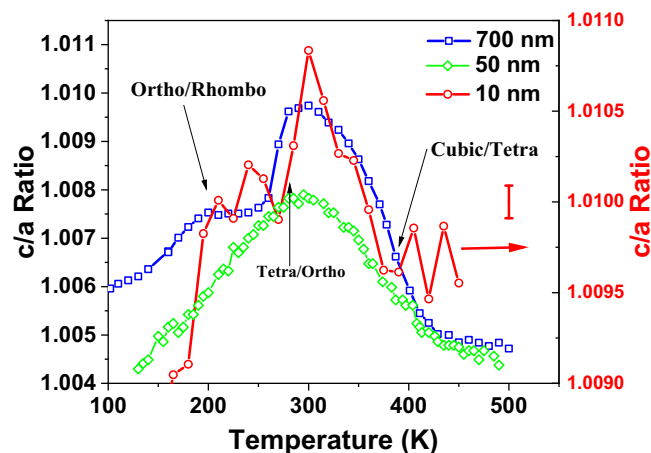
FIG. 5. The c/a lattice parameter ratio of the 700-nm (blue), 50-nm (green), and 10-nm (red) BaTiO$_3$ core-shell nanoparticles. The left y axis is for the 700- and 50-nm reference samples, and the right y axis for the 10-nm milled sample. The error bars are at the level of the scattering of the points in the dense data for the 700- and 50-nm systems. An estimated upper limit error (red bar) is given for the 10-nm sample.

from unity (right scale of Fig. 5) exists for the temperate range ≈ 150 to ≈ 500 K. These results suggest that the 10-nm sample possesses a strong bulklike behavior including stabilization of the polar ferroelectric phase.

IV. SUMMARY

BaTiO$_3$ nanoparticles (≈ 10 nm) prepared by ball-milling in oleic acid are studied together with unmilled 50- and 700-nm (bulk) particles as a reference. Raman spectroscopy, laboratory XRD, synchrotron-based XAFS, and PDF analysis have been conducted to understand the structural mechanism behind the unusually large electric polarization in the nanoparticles. Compared to free-standing barium oleate, the corresponding component in the 10-nm sample matrix exhibits sharp Raman peaks consistent with a highly crystalline form, which is presumed to be crystalline organic coating (shell) around the BaTiO$_3$ core with a coating to core ratio

of $\approx 0.7 \pm 0.1 : 1.0$ by volume. Local structural measurements show large Ti off-centering in the milled 10-nm samples [enhanced beyond orthorhombic (bulk) BaTiO$_3$]. Moreover, bulklike sharp structural transitions are observed in the milled 10-nm nanoparticles, in contrast to the 50-nm unmilled nanoparticles. A complex crystalline BaTiO$_3$/Ba oleate type composite material exists, which stabilizes a high a/c lattice asymmetry and, in turn, generates a strong ferroelectric effect.

Considering this nanoparticle system to be core shell in configuration, the recovery of bulklike behavior is attributed to stress provided by the barium oleate outer shell, i.e., a lattice mismatch between the crystalline organic shell and inorganic core, which is responsible for sustaining and enhancing the ferroelectric effect (spontaneous polarization) in these nanoparticles. Surface stress is demonstrated experimentally by Cook *et al.* in Ref. [10]. Surface stress-enhancing ferroelectric properties is supported theoretically by Morozovska *et al.* (Ref. [9]) and Ederer and Spaldin (Ref. [45]). Both in-plane compression and in-plane tension are known to enhance ferroelectricity in BaTiO$_3$ thin films [46]. The same mechanism is expected in this case. We note that studies of CoFe$_2$O$_4$ nanoparticles reveal that oleic acid molecules bond to metal sites on the surface of the particles and produce surface strain resulting in enhanced coercivity [47,48]. In the case of BaTiO$_3$, the strain enhances the Ti off-centering resulting in an enhanced spontaneous polarization.

[1] N. Nuraje and K. Su, Nanoscale **5**, 8752 (2013).

[2] M. Polking, M.-G. Han, A. Yourdkhani, V. Petkov, C. F. Keselowski, V. V. Volkov, Y. Zhu, G. Caruntu, A. P. Alivisatos, and R. Ramesh, Nat. Mater. **11**, 700 (2012).

[3] F. Kruis, H. Fissan, and A. Peled, J. Aerosol Sci. **29**, 511 (1998).

[4] G. Reiss and A. Hutten, Nat. Mater. **4**, 725 (2005).

[5] J. Mangeri, Y. Espinal, A. Jokisaari, S. P. Alpay, S. Nakhmanson, and O. Heinonen, Nanoscale **9**, 1616 (2017).

[6] W. Zhang, Y. Xue, Q. Fu, Z. Cui, and S. Wang, Powder Technol. **308**, 258 (2017).

[7] E. K. Akgodan and A. Safari, Jpn. J. Appl. Phys. **41**, 7170 (2002).

[8] K. Ishikawa, K. Yoshikawa, and N. Okada, Phys. Rev. B **37**, 5852 (1988).

[9] A. N. Morozovska, M. D. Glinchuk, and E. A. Eliseev, Phys. Rev. B **76**, 014102 (2007).

[10] G. Cook, J. L. Barnes, S. A. Basun, D. R. Evans, R. F. Ziolo, A. Ponce, V. Yu. Reshetnyak, A. Glushchenko, and P. P. Banerjee, J. Appl. Phys. **108**, 064309 (2010).

[11] Z. Zhao, V. Buscaglia, M. Viviani, M. T. Buscaglia, L. Mitoseriu, A. Testino, M. Nygren, M. Johnsson, and P. Nanni, Phys. Rev. B **70**, 024107 (2004).

[12] S. A. Basun, G. Cook, V. Yu. Reshetnyak, A. V. Glushchenko, and D. R. Evans, Phys. Rev. B **84**, 024105 (2011).

[13] Y. Reznikov, O. Buchnev, O. Tereshchenko, V. Reshetnyak, A. Glushchenko, and J. West, Appl. Phys. Lett. **82**, 1917 (2003).

[14] H. Atkuri, G. Cook, D. R. Evans, C.-I. Cheon, A. Glushchenko, V. Reshetnyak, Yu. Reznikov, J. West, and K. Zhang, J. Opt. A: Pure Appl. Opt. **11**, 024006 (2009).

[15] D. R. Evans, S. A. Basun, G. Cook, I. P. Pinkevych, and V. Yu. Reshetnyak, Phys. Rev. B **84**, 174111 (2011).

[16] Yu. A. Barnakov, I. U. Idehenre, S. A. Basun, T. A. Tyson, and D. R. Evans, R. Soc. Chem., Nanoscale Adv. **1**, 664 (2019).

[17] G. Cook, A. V. Glushchenko, V. Reshetnyak, A. T. Griffith, M. A. Saleh, and D. R. Evans, Opt. Express **16**, 4015 (2008).

[18] G. Cook, V. Yu. Reshetnyak, R. F. Ziolo, S. A. Basun, P. P. Banerjee, and D. R. Evans, Opt. Express **18**, 17339 (2010).

[19] R. K. Shukla, C. M. Liebig, D. R. Evans, and W. Haase, R. Soc. Chem., RSC Adv. **4**, 18529 (2014).

[20] R. K. Shukla, D. R. Evans, and W. Haase, Ferroelectrics **500**, 141 (2016).

[21] I. U. Idehenre, Yu. A. Barnakov, S. A. Basun, and D. R. Evans, J. Appl. Phys. **124**, 165501 (2018).

[22] A. R. Stokes and A. J. C. Wilson, Proc. Cambridge Philos. Soc. **38**, 313 (1942).

[23] A. A. Coelho, J. Appl. Crystallogr. **33**, 899 (2000).

[24] See Supplemental Material at http://link.aps.org/supplemental/10.1103/PhysRevB.108.064106 for details on sample preparation, experimental and simulation methods, and additional structural and spectroscopic information.

[25] Y. Numata, H. Kobayashi, N. Oonami, Y. Kasai, and H. Tanaka, J. Mol. Struct. **1185**, 200 (2019).

[26] M. Marssi and R. Farhi, J. Appl. Phys. **80**, 1079 (1996).

[27] G. Sokrates, *Infrared and Raman Characteristic Group Frequencies* (John Wiley and Sons, Chichester, 2001).

[28] T. A. Tyson, T. Yu, M. Croft, M. E. Scofield. D. Bobb-Semple, J. Tao, C. Jaye, D. Fischer, and S. S. Wong, Appl. Phys. Lett. **105**, 091901 (2014).

[29] A. I. Frenkel, D. Ehre, V. Lyahovetskaya, L. Kanner, E. Wachtel, and I. Lubomirsky, Phys. Rev. Lett. **99**, 215502 (2007).

[30] J. C. Woicik, E. L. Shirley, C. S. Hellberg, K. E. Andersen, S. Sambasivan, D. A. Fischer, B. D. Chapman, E. A. Stern, P. Ryan, D. L. Ederer, and H. Li, Phys. Rev. B **75**, 140103 (2007).

[31] B. Ravel and E. A. Stern, Phys. B (Amsterdam, Neth.) **208–209**, 316 (1995).

[32] Q. Qian, T. A. Tyson, M. Deleon, C. C. Kao, J. Bai, and A. I. Frenkel, J. Phys. Chem. Solids **68**, 458 (2007).

[33] Q. Qian and T. A. Tyson, Appl. Phys. Lett. **80**, 3141 (2002).

[34] Q. Qian, T. A. Tyson, S. Savrassov, C. C. Kao, and M. Croft, Phys. Rev. B **68**, 014429 (2003).

[35] V. Vedrinskii, V. L. Kraizman, A. A. Novakovich, Ph. V. Demekhin, and S. V. Urazhdin, J. Phys.: Condens. Matter **10**, 9561 (1998).

[36] T. A. Tyson, Phys. Rev. B **49**, 12578 (1994); (unpublished software package).

[37] M. O. Krause and J. H. Oliver, J. Phys. Chem. Ref. Data **8**, 329 (1979).

[38] G. H. Kwei, A. C. Lawson, S. J. L. Billinge, and S.-W. Cheong, J. Phys. Chem. **97**, 2368 (1993); R. H. Buttner and E. N. Maslen, Acta Crystallogr., Sect. B **48**, 764 (1992).

[39] R. B. Neder and T. Proffen, *Diffuse Scattering and Defect Structure Simulations* (Oxford University Press, Oxford, 2008).

[40] T. Egami and S. L. J. Billinge, *Underneath the Bragg Peaks: Structural Analysis of Complex Materials* (Pergamon, Amsterdam, 2003).

[41] T. Proffen, S. J. L. Billinge, T. Egami, and D. Louca, Z. Kristallogr. **218**, 132 (2003).

[42] V. Petkov, *Characterization of Materials* (Wiley-Interscience, Hoboken, NJ, 2003).

[43] C. L. Farrow, P. Juhas, J. W. Liu, D. Bryndin, E. S. Božin, J. Bloch, Th. Proffen, and S. J. L. Billinge, J. Phys.: Condens. Matter **19**, 335219 (2007).

[44] M. B. Smith, K. Page, T. Siegrist, P. L. Redmond, E. C. Walter, R. Seshadri, L. E. Brus, and M. L. Steigerwald, J. Am. Chem. Soc. **130**, 6955 (2008).

[45] C. Ederer and N. Spaldin, Phys. Rev. Lett. **95**, 257601 (2005).

[46] K. J. Choi, M. Biegalski, Y. L. Li, A. Sharan, J. Schubert, R. Uecker, P. Rieche, Y. B. Chen, X. Q. Pan, V. Gopalan, L.-Q. Chen, D. G. Schlom, and C. B. Eom, Science **306**, 1005 (2004).

[47] M. V. Limaey, S. B. Singh, S. K. Date, D. Kothari, V. R. Reddy, A. Gupta, V. Sathe, R. J. Choudhary, and S. K. Kulkarin, J. Phys. Chem. B **113**, 9070 (2009).

[48] S. Jovanovic, M. Spreitzer, M. Tramsek, Z. Trontelj, and D. Suvorov, J. Phys. Chem. C **118**, 13844 (2014).